Surface microstructure of an IN718 3D coating manufactured by Laser Metal Deposition

Theo Zurcher, Vincent Fridrici, Eric Charkaluk

To cite this version:

Theo Zurcher, Vincent Fridrici, Eric Charkaluk. Surface microstructure of an IN718 3D coating manufactured by Laser Metal Deposition. Materials Characterization, 2023, 203, pp.113054. 10.1016/j.matchar.2023.113054 . hal-04289610

HAL Id: hal-04289610
https://hal.science/hal-04289610v1

Submitted on 16 Nov 2023

Surface microstructure of an IN718 3D coating manufactured by Laser Metal Deposition

Theo Zurcher[1,2,*], Vincent Fridrici[2], and Eric Charkaluk[1]

[1]Ecole Polytechnique, Laboratoire de Mécanique des Solides, UMR CNRS 7649, 91120 Palaiseau, France

[2]Ecole Centrale de Lyon, Laboratoire de Tribologie et Dynamique des Systèmes, UMR CNRS 5513, 69130 Ecully, France

[*]theo.zurcher@polytechnique.edu

Keywords: Additive Manufacturing, Laser Metal Deposition, Repair, Surface, Microstructure, EBSD

Abstract

Laser Metal Deposition (LMD) is a well-known additive manufacturing (AM) process that offers the ability to repair metal parts, among other benefits. We have focused on IN718 parts that evolve in environments that strongly favor wear. Therefore, a good knowledge of the contact surface microstructure and its properties is necessary to better understand the tribological behavior of these parts. However, the microstructure of the top surface (which is most susceptible to wear) of IN718 coatings deposited by LMD is not particularly well documented in the literature. Most of the studies devoted to this alloy have focused on the study of the cross-sectional microstructure, and the few articles dealing with the top surface microstructure have been devoted to the Laser Powder Bed Fusion (LPBF) process. In this article, four IN718 coatings were successfully fabricated with high density using different scanning strategies. When viewing the microstructure from the top surface, the EBSD map showed a very heterogeneous microstructure with an alternation of fine and coarse grains. It also showed a weak overall texture, but a strong local texture within the fine and coarse grain region. EBSD analysis of the cross-sectional area of the coated section also revealed a microstructure variation along the build direction (BD) with the appearance of small grains between layers after some layers have been deposited. Analysis of both sides of the coated part allowed us to get a better understanding of the final microstructure. We were able to show that this heterogeneous microstructure leads to a spatial variation of the top surface hardness, the pattern of which is directly related to the scanning strategy. Finally, we found that the surface hardness of IN718 LMD samples is higher than that of conventionally produced IN718, which is a promising result in terms of repairing metal parts with good tribological properties.

1 Introduction

As the environmental crisis is more than ever a hot topic, the repairs of metallic parts are increasingly studied to save resources. It exists several processes to repair metallic parts which have been worn out during their service such as the thermal spray [1], arc welding [2], cold spray [3] etc. Some additive manufacturing (AM) processes offer also the possibility to restore worn-out parts. The use of AM as a repairing process offers the benefit of reducing the high machining cost through highly accurate deposition on complex geometric parts. Most of those techniques belong to the family of the Direct Energy Deposition (DED) process. Laser Metal Deposition (LMD) is one of the most known and studied DED processes. LMD uses metallic powder as feedstock material. A moving coaxial nozzle conveys powder through a laser beam that melts the latter and then solidifies to form a bead. This way of repairing is based on an addition of beads next to each other and by repeating this method layer by layer. It allows the restoration of small local defects. Usually, before repairing those defects, the worn-out area of the piece is machined to have a sound basis to fill in [4]. The LMD process can also be used to coat worn surfaces with a harder material. Thus, the deposited coating can protect the original weaker material and so increases the sustainability of the piece [5]. Finally, this process can fully restore pieces that have been damaged during their service life. For instance, turbine blades can be repaired using LMD [6] or sprockets of a mining machine can be restored [7]. Bi et al. and Unal-Saewe et al. successfully repaired a turbine blade by depositing a nickel-based superalloy with the LMD process [8, 9].

IN718 is one of the most studied alloys in additive manufacturing because of its good weldability and its wide use in the aerospace field. It offers high mechanical properties and good corrosion resistance up to 650°C [10]. At this temperature, yield strength and the ultimate tensile strength are around 1000 MPa and 1300 MPa respectively [11]. Currently, aircraft engines see most of their metallic components used at high temperatures (such as turbine blades, disks, shafts, stators, and casing...) made up of this alloy. IN718 is a nickel-based superalloy strengthened by the precipitation of coherent intermetallics γ' and γ'' inside the austenitic matrix γ. After homogenization and double aging heat treatment, the conventional manufactured IN718 microstructure consists of equiaxed grains surrounded by δ phase along the grains boundaries with strengthening phases scattered in the microstructure. The δ phase plays a crucial role by pinning grain boundaries and thus inhibiting grain growth. Some carbides (mainly NbC), borides, and titanium nitrides are also noticed sporadically.

IN718 deposited by LMD has a highly metastable microstructure because of the high cooling rate (close to $10^3\ °C/s$). Most of the studies report the micro-segregation of a large amount of high atomic elements (such as Nb and Mo) in the interdendritic region leading to the precipitation of Laves phases [12]. The brittleness of those phases is detrimental to the mechanical properties of this alloy. Due to the sluggishness of the precipitation kinetics of strengthening phases, the latter is not detected in the matrix [13–16]. Moreover, the excessive number of Laves phases traps the Nb needed for the precipitation of $\gamma'' - Ni_3Nb$ strengthening phase. It is worth noting that some articles [17, 18] observed, by using transmission electron microscopy (TEM) or high-resolution scanning electron microscopy (SEM), very few strengthening phases in the matrix as-deposited samples because of the high energy employed to build their samples. The grains are mainly columnar with a dendritic/cellular sub-microstructure with a growth direction along $\langle 100 \rangle$ crystallographic orientation which is aligned with the building direction (BD) [19]. By investigating the microstructure of a single bead wall, some authors showed that the process parameters (especially laser power, scanning speed, and strategy) could highly impact the microstructure [13, 14]. As commonly observed in AM processes, the microstructure consists of columnar grains growing epitaxially from the previously deposited layer following the ⟨100⟩ direction which is the preferred growth direction of the fcc Ni-superalloy. However, they noticed that process parameters could change grain morphology and the overall texture. Guevenoux et al. [20] highlighted the significant impact of the dwell time on the microstructure. Depending on the increase of dwell time, the microstructure could be either highly columnar and textured or have a herringbone pattern of columnar grains with a weaker texture. Yuan et al. [21] also pointed out the larger primary dendrite space as the energy density increases. Therefore, the thermal history of repaired part by LMD are greatly influenced by process parameters. By choosing a suitable set of parameters and possible thermomechanical treatments during or after the process, it is possible to tailor the microstructure to obtain optimized mechanical properties. For example, it has been shown that LMD process associated to an ultrasonic vibration system allows the refinement of the microstructure by a cavitation phenomenon inside the melt pool [22] conducting to better mechanical and tribological properties as well as density of IN718 parts [23].

The mechanical properties induced by these microstructures have been widely studied in the literature [16, 20, 21, 24, 25]. Due to the columnar morphology of grains and the strong {100} texture, as-built LMD repairs have anisotropic macroscopic mechanical properties [26]. Sui et al. [24] showed that the Laves phases inside the austenitic matrix could be either beneficial or detrimental for fatigue resistance according to their morphology and the stress amplitude. Yuan et al. [21] investigated the impact of microstructure on mechanical properties after several heat treatments. They noticed that mechanical anisotropy virtually disappears after full heat treatment (homogenization, solution, and aging). Generally, studies showed that as-deposited samples have lower tensile strength compared to wrought ones [16, 24, 27]. However, after appropriate heat treatment, those repairs could have sometimes even better mechanical properties than the conventionally manufactured IN718 [27].

For the sake of the investigation of mechanical properties caused by the inherent microstructure of the LMD process, most of the studies focused on the observation of the microstructure of the cross-sections parallel to the BD [14, 16, 20, 25, 28]. Furthermore, studies on the LMD IN718 microstructure are common in the literature but most of them focused their studies on single bead walls to answer the need for repairing thin turbine blades [14, 15, 20]. However, some defects need larger three dimension repairs. By adding a third dimension to the building, the microstructure is greatly affected [16, 21]. Stevens et al. [18] studied the microstructure and the hardness of laser-deposited cuboids in IN718 on different surfaces of the building. They observed a change in hardness and Laves phase fraction depending on how far the measurements are from the top surface. Bahshwan et al. highlighted the crucial role of the microstructure features on the wear properties of stainless steel printed by laser powder bed fusion (LPBF) [29]. Yang et al. also revealed how the cellular sub-microstructure induced by the high cooling rate of AM process plays a role in wear resistance [30]. They demonstrated an anisotropic wear behavior caused by the microstructure. Those articles show that having a deep understanding of the contact surface microstructure is highly required in some cases such as mechanical contact studies.

From this short literature review, it can be raised that, to our knowledge, the study of the microstructure of the top surface of a 3D coatings deposited by LMD was not undertaken. Most of the article studying the top surface microstructure focused their work on the LPBF process and on other alloy grades (such as the 316L stainless steel) [29, 30]. Furthermore, the very few articles studying

IN718 microstructures induced by LMD focused exclusively on cross-sectional faces [18]. Thus, the objective of this work concerns a deep investigation of IN718 top surface microstructures obtained by LMD and contributes to obtaining further information about its formation. Based on this investigation, the ultimate goal is to give resources to be able to tailor, in a near future, wear-resistant coatings through the LMD process.

More precisely, in this work, we investigate from several points of view the microstructure of IN718 3D-coated parts according to four different scanning strategies. First, the sample's density is examined by image analysis. Then, large electron backscattered diffraction (EBSD) cartographies of the top and lateral sample cross-sections are analyzed for a better understanding of the induced microstructure. Grain size, morphology as well as textures at different scales, are particularly examined. Finally, microhardness is investigated to reveal the impact of the microstructure on local mechanical properties.

2 Materials and method

2.1 Powder materials and laser processing

IN718 coatings were fabricated using a DED *Mobile* machine from BeAM [31]. This 3D printer is equipped with a 500 W YLR-fiber laser. A three-interlocked cones nozzle in which argon gas passes conveys the powder near the focal point of the laser. Before the building, the nozzle is positioned at 3.5 mm from the surface of the substrate which results in having a laser spot diameter of 0.74 mm. The commercially available IN718 powder was provided by Oerlikon [32] and was produced by gas atomization.

Granulometry			Apparent density (Hall cup)	Flowrate
d_{10}	d_{50}	d_{90}		
50 µm	67 µm	107 µm	4 g/cm^3	16 s/50g

Table 1: Properties of the IN718 powder

Elements	Ni	Fe	Ti	Al	Nb	Co	Cr	Mo	Mn	C	N	Si
weight%	Bal.	18.25	0.92	0.42	5.15	0.05	18.92	3.11	0.1	0.05	0.03	0.03

Table 2: Chemical composition of the IN718 powder

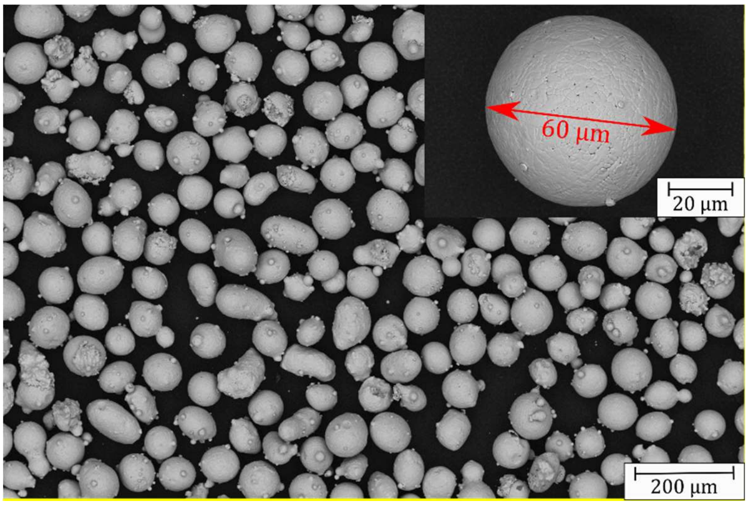

Figure 1: Morphology of the IN718 powder used to manufacture the samples

The particle size range is between 45 and 115 µm. The morphology of the IN718 powder is shown in Fig 1. Most of the powder particles are spherical and they are, sometimes, surrounded by some satellites. Further information about the powder features and composition are respectively displayed in Tables 1 and 2. The samples were printed on the same substrate made up of low-alloyed steel XC48. This steel grade was chosen because of its large use in some industries (construction, railway...). In total, four parallelepipeds have been fabricated on a 200×150×8 *mm* steel substrate. The four buildings were separated by using a bandsaw to finally get 85 × 65 *mm* repaired plates as shown in Fig 2.

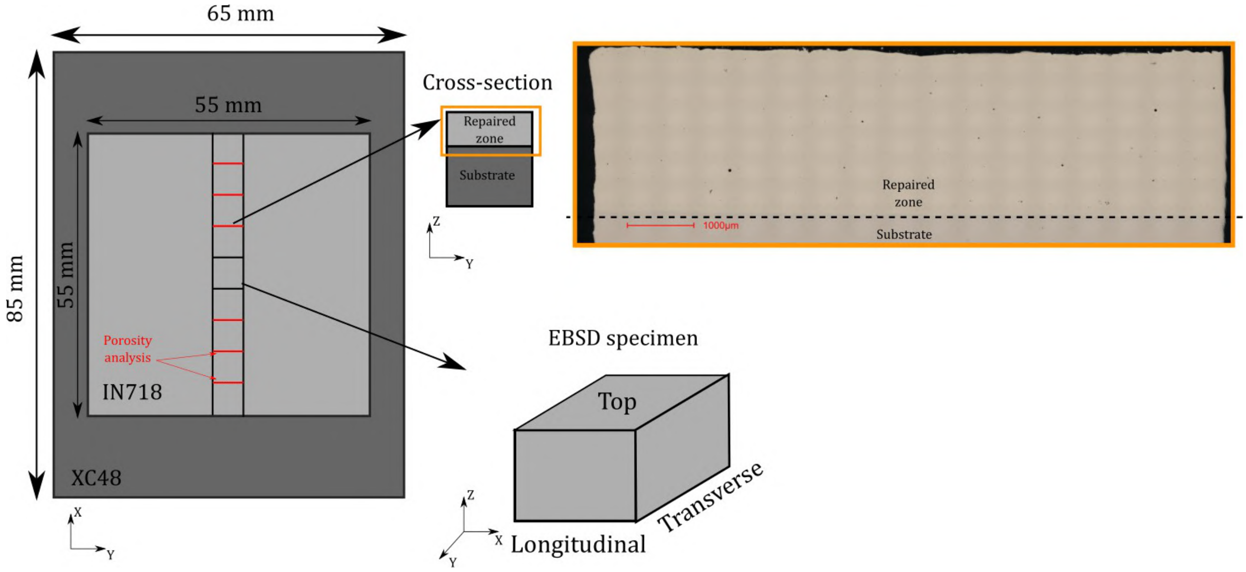

Figure 2: Sample plan showing analysis location

The goal was to obtain dense 55 × 55 × 1.5 *mm* coatings (density over 99%). To achieve it, a three steps parametric study was implemented. First of all, the cross-sections of single beads (built with a different set of parameters) were analyzed. The selection of parameter sets was based on different geometrical criteria of the bead which are: a dilution of the bead (which is the ratio between the diluted area of the bead over the total area of the bead) in the substrate between 10 and 30 percent [33], a clad angle above 100° [5] and the absence of unmelted powder on the top of the bead [34]. The second step consisted of the building of 3D coatings with the selected parameters by varying the overlap rate to end up with the denser coating as possible. Then, the choice of the optimal set of parameters was undertaken in the final step. Finally, the coatings have been performed in a free atmosphere using a laser power of 325 W, a scanning speed of 2250 mm/min, a powder rate flow of 7 g/min, a 0.2 mm vertical increment of the nozzle at every new layer and an overlap rate of 30 percent. The only varying parameter among the samples is the scanning strategy. Each sample was built by using a unique path of the laser. The four different strategies studied in this work are exhibited in Fig 3. Each strategy consists of a back-and-forth scanning motion of the laser with a variable angle of rotation for each new layer. As explained in Fig 3 a), sample S0 consists of a simple addition of layers without any rotation of the scanning direction between layers. S45 and S90 consist of an incremental rotation of 90° at each layer. They are differentiated by the initial direction of the scanning path. For the S90, the scanning direction is along the borders of the substrate while the S45 initial scanning direction is rotated by 45°. Those strategies are shown in Fig 3 b) and d) respectively. The last strategy illustrated in Fig 3 c), consists of an incremental rotation of 67° for every new layer. This strategy is well known for its capability of reducing mechanical anisotropy along with residual stresses [35–37]. So this strategy could be interesting when it comes to applying coatings with limited number of post-treatment steps.

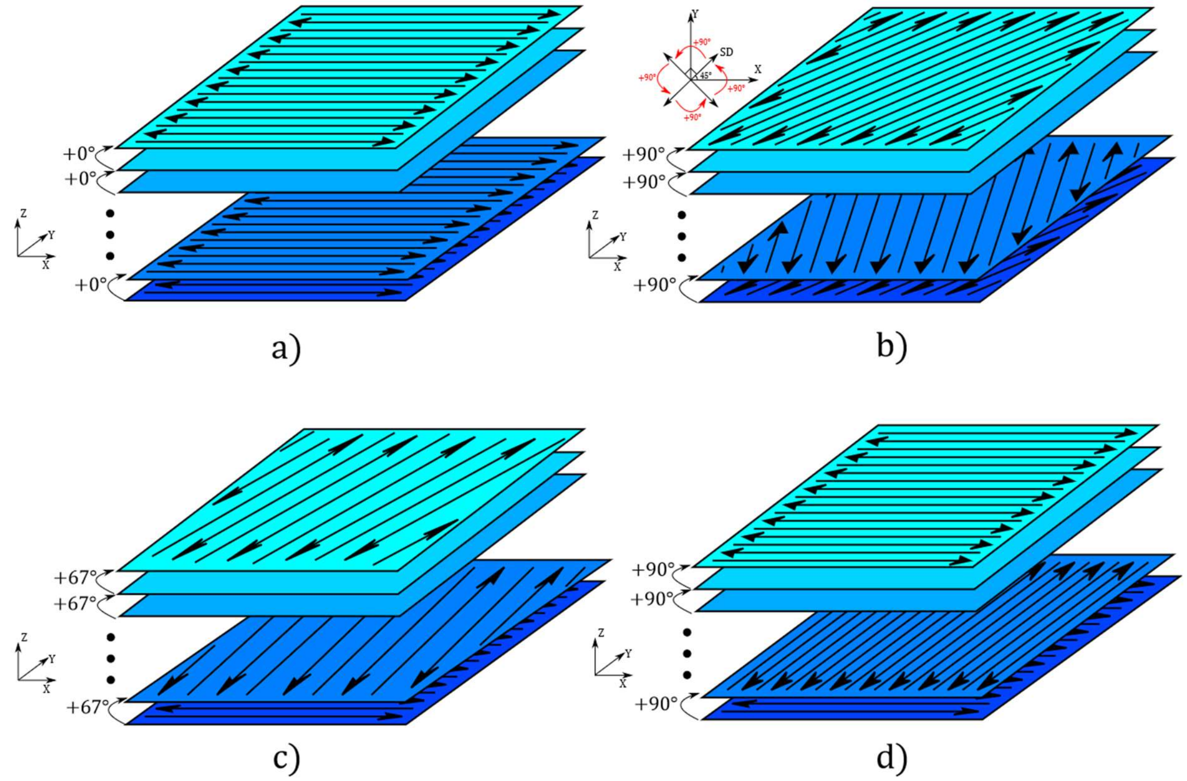

Figure 3: The four different scanning strategies employed for coatings: a) S0 ; b) S45 ; c) S67 ; d) S90.

2.2 Experimental characterization

2.2.1 EBSD analysis

Before microstructure analysis, specimens were polished by using silicon carbide abrasive papers with grit values from 600 to 4000 and finished with successively diamond paste of 3 μm and 1 μm. Finally, to ensure optimal diffraction of grains and to get rid of the strain induced by the mechanical polishing, an ion polished protocol was done with a *PECS II* machine from Gatan. It involves focusing a 6 keV argon ion beam with an incidence angle of 9°on rotating samples (6 rpm) for 15 min.

To perform a quantitative analysis of the inherent microstructure of the sample, Electron BackScaterred Diffraction (EBSD) cartographies were acquired. An FEI *QUANTA 600F* SEM (Scanning Electron Microscopy) apparatus equipped with an EBSD camera from Oxford Instrument was used to perform those measurements. The acquisitions were performed under a beam voltage of 30 kV. The step size was set at 0.6 µm. The data were analyzed on Aztec and Channel5 softwares [38]. As explained in Fig 2, we name as top, transverse and longitudinal surfaces, the ones which belong to the XY, YZ, and XZ planes respectively. To have a macroscopic view of the microstructure and a high amount of grains, large EBSD maps of the top surface were acquired in the middle of the sample as shown in Fig 2. The studied surface varies between 8 and 12 mm^2. Those maps are the combination of several 350 × 500 μm maps stitched together. Some EBSD maps of the transverse faces of coatings were also performed with a studied area of 6 mm^2. Additionally, to compare the IN718 microstructures of our coatings with IN718 conventionally manufactured, an EBSD map of a wrought sample was acquired as well following the same protocol.

The segmentation angle which describes the grain boundaries was defined at 10° and the smallest grains have an area of 1,8 μm^2. To study grain morphology, two geometrical features of the grains have been investigated. The size is measured by the equivalent circle diameter d_{eq}. The latter represents the diameter of a fitted circle for each grain. The shape of the grain is characterized by the aspect ratio which is calculated by dividing the major axis of a fitted ellipse of the grain by its minor axis. A statistical study of the size and morphology of the grains was performed. According to their distributions, the probability distribution functions were fitted with a log-normal law.

2.2.2 Density measurement

Those measurements aim to compare the density between the four samples and to evaluate the set of parameters chosen for coating. As absolute density is not needed, we chose to carry out our measurement by using a 2D image analysis method. Although it gives no information on the absolute density, it allows us to quickly compare the density between different samples without using advanced density measurement apparatus such as tomography. To fairly compare the density of samples, the same routine analysis was applied to an equal area for all samples. The stitched pictures were analyzed with *ImageJ*. The density of the sample was measured by analyzing the transversal cross-sections at six different locations in the samples as illustrated in Fig 2. Each face represents an area of 20 mm^2 which gives a total analyzed area of 120 mm^2. Each face was mechanically polished until the finishing step with a 3 μm diamond paste. To detect the smallest porosities, the pictures acquired with a numerical microscope Keyence *VHX6000* were taken with a ×400 magnification. The smallest picked-up porosity has an area of 2,5 μm^2. The pictures were automatically stitched thanks to the microscope software.

2.2.3 Hardness measurement

Vickers hardness (HV) measurements were realized on the same faces where the EBSD maps were done. A *Zwick* micro-indentor was used to carry out a ten-by-ten indentation matrix. The indentations were separated by 100 μm. The applied load was 750 mN for 5 seconds which results in an indent with a diagonal of approximatTaely 20 μm. In addition, hardness profiles from the transversal face of the coatings were performed to detect any hardness variation along the building direction. The indentations were performed with the same parameters. The distance between each indentation was set to 50 μm.

3 Results

3.1 Porosity

Porosity measurement is used as an optimization criterion to select building parameters. Different kinds of pores can be observed in AM parts. Porosities caused by trapped gas in the melt pool are easily recognized by their spherical shape. Bad quality of powder or a non-optimized choice of building parameters can be the reason for such pores. Then," sharp angle" pores called lack of fusion can be also reported. Their angular shape makes them preferential sites of crack initiation. It's well-known that high amount of porosities is highly detrimental to the mechanical properties of the coated part [39]. It has been shown that angular defects due to lack of fusion greatly impact the fatigue life of the LMD coatings [40]. The nature of the pores observed in our samples is mostly spherical. However, as shown in Fig 4, very few lacks of fusion can be noticed. Regardless of those pores, Table 3 highlighted the high density of the repaired area. It has been estimated that all samples have a density close to 99,9 %. As previously explained, those values are probably slightly overestimated. Nonetheless, it shows that the scanning strategy does not affect the density. As a consequence, regardless of the scanning employed strategy, our set of parameters chosen to deposit IN718 has given rise to dense and healthy coatings.

Samples	S0	S45	S67	S90
Density (%)	99.91±0.04	99.91±0.04	99.92±0.01	99.90±0.03

Table 3: Samples' density

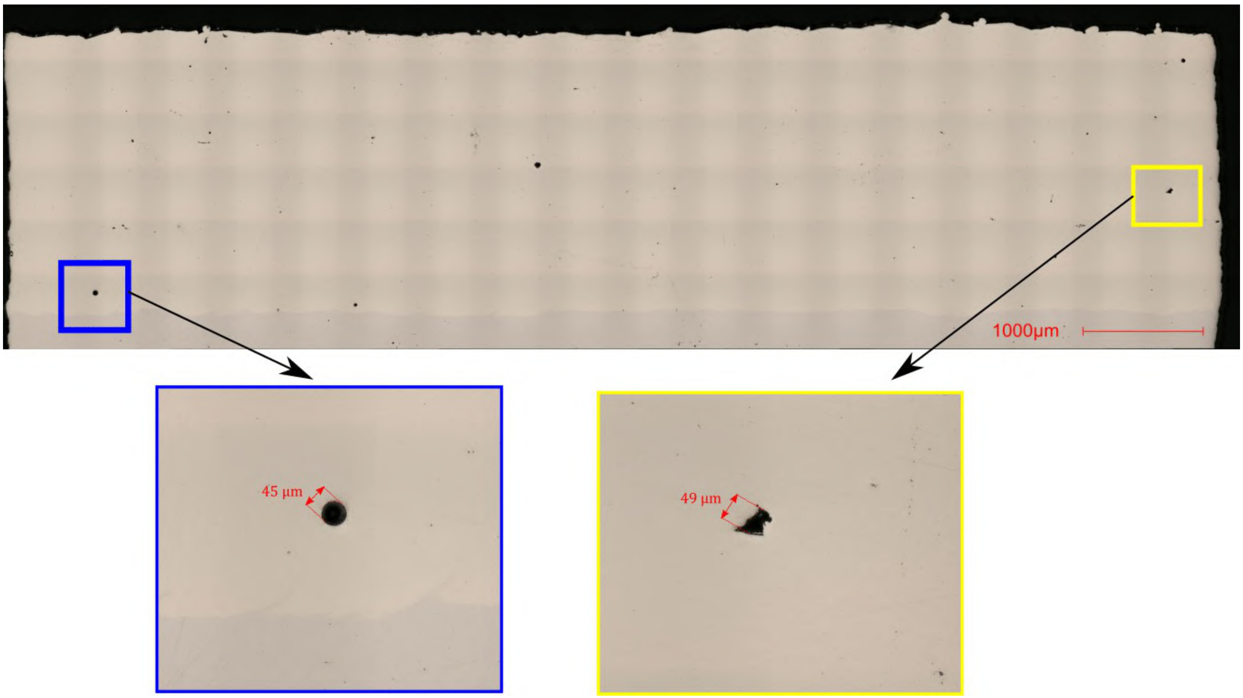

Figure 4: Type of porosities observed in one of the analyzed slices belonging to S67 sample

3.2 Microstructure

To simplify the discussion and given their similarities, only the S0 and S45's microstructures will be exhibited. For information, S67 and S90 have similar microstructures (see Table 4) except for one difference which is the grain layout caused by the different laser paths.

3.2.1 EBSD of the coatings transversal face

A well-studied type of EBSD map (IPF Z) is shown in Fig 5 a). It corresponds to the transverse face of the coated area of S0. An epitaxial grains growth within the first three deposited layers can be observed (delimited by the red dotted line in Fig 5 a)). Above, the epitaxial growth appears to be hindered by small grains. A zoom allows exhibiting the beads which were highlighted with white dotted lines in Fig 5 b). The growth of the grains of each bead starts epitaxially from clusters of small grains at the top of the previously deposited layer. One can see that grains on bead sides seem to have their ⟨110⟩ and ⟨111⟩ direction mainly oriented along the BD while the grains located in the middle of the bead see their ⟨100⟩ direction aligned with the BD. Also, as it can be observed in Fig 5 c), the texture is relatively weak for a microstructure inherited from an AM process.

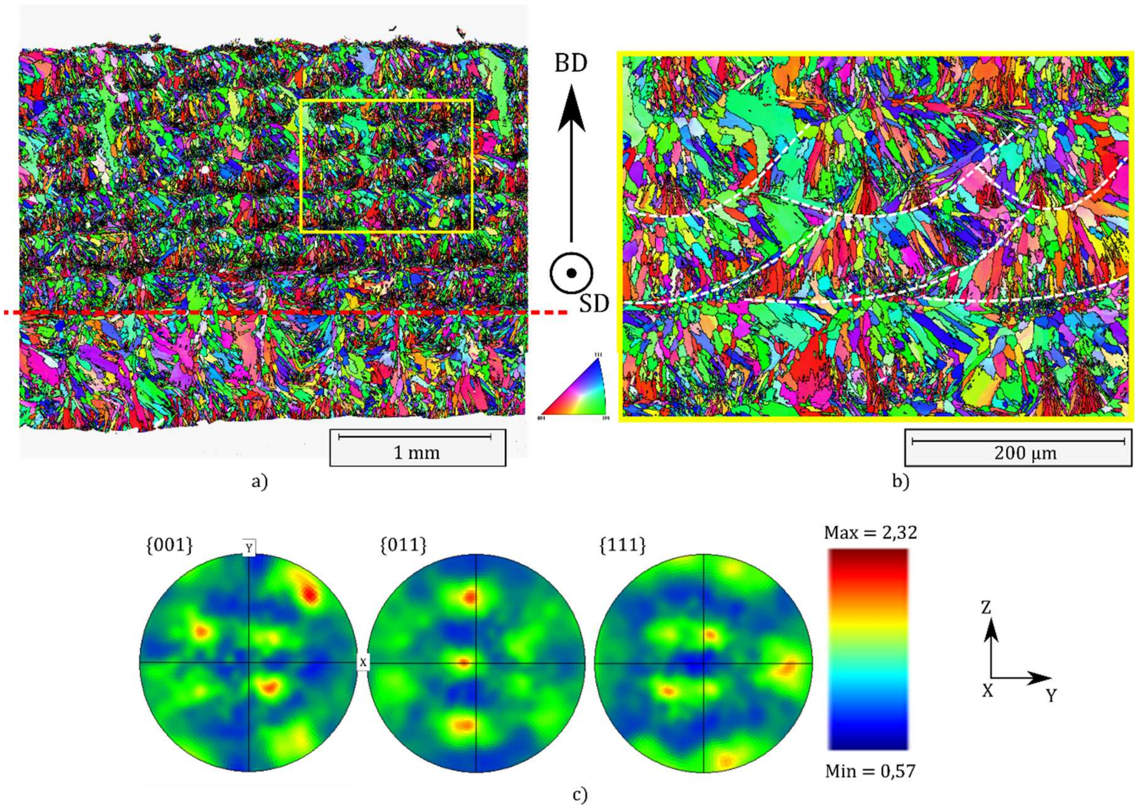

Figure 5: a) IPF Z showing the subsets taken off from the transversal surface of S0; b) A zoomed-in area highlighting (yellow frame) several beads with black dotted lines; c) Pole figures of unzoomed transversal EBSD map

3.2.2 EBSD of the coatings top surface

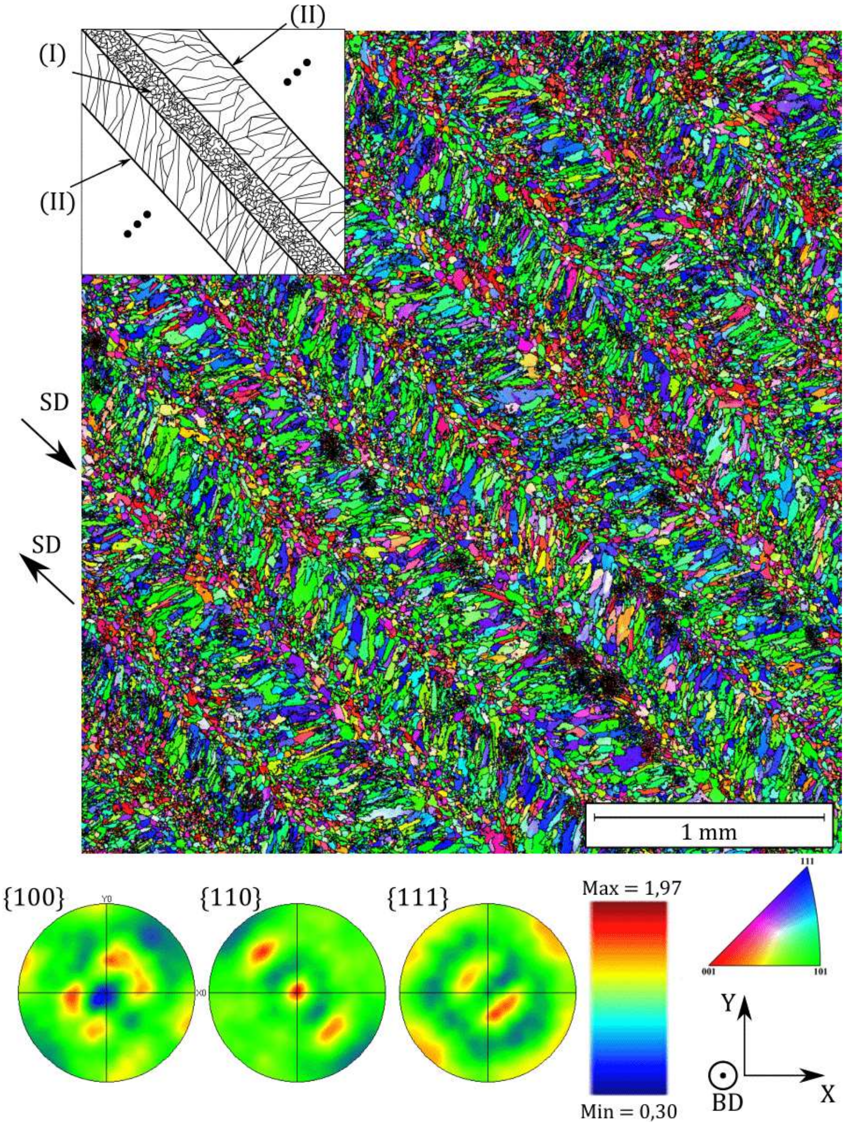

Figure 6: IPF Z showing the top surface of S45 and its pole figures

The top surface's inverse pole figure (IPF) according to Z direction (which is aligned with the BD) and its pole figures are presented for S45 in Fig 6. From an overall point of view, laser passes can be observed through this EBSD map. The microstructure consists of the alternation of fine equiaxed grains (I) and coarse columnar grains (II). If we focus on the microstructure of one single bead, its microstructure is similar to a welding joint [41]. Grain inclination follows the direction of the laser which leads to this herringbone pattern of the grains periodically divided by small equiaxed grains (I). A deeper investigation of the origin of the grain morphology will be done further in this paper.

It can be seen that, as with the transverse face, the overall texture is quite weak, with a maximum of Multiples of Uniform Density (MUD) around 2, which is the same for all samples (see Table 4). To discriminate between both microstructures, we established a grain size threshold that corresponds to the smallest grains observed in the large columnar grains in S0. Based on this criterion, the threshold has been set to 25 μm. The statistical data on the grain size and morphology are summarized in Table 4. It is worth noting that on average, for all the samples, the small grain size population occupies a bit less than half of the total surface but represents 90% of the number of grains. Furthermore, for all the studied strategies, the average grain size is about 7 μm and 30 μm for small and large grains respectively. Table 4 confirms the fact that the larger grains are more likely to get a columnar shape than small grains. Indeed, despite the large standard deviation, the average aspect ratio of the coarse grains is greater than the one of the small grains. This result is reinforced by the analysis of the whiskers diagrams of the grains aspect ratio exhibited in Fig 7. It clearly shows that the third quartile and the last extremity of the whiskers diagrams (which represents 1.5 times the interquartile space) of the large grains are more extended towards the high aspect ratio than for the small ones. Finally, Fig 7 highlights also the strong degree of similarity of grain morphology between each strategy.

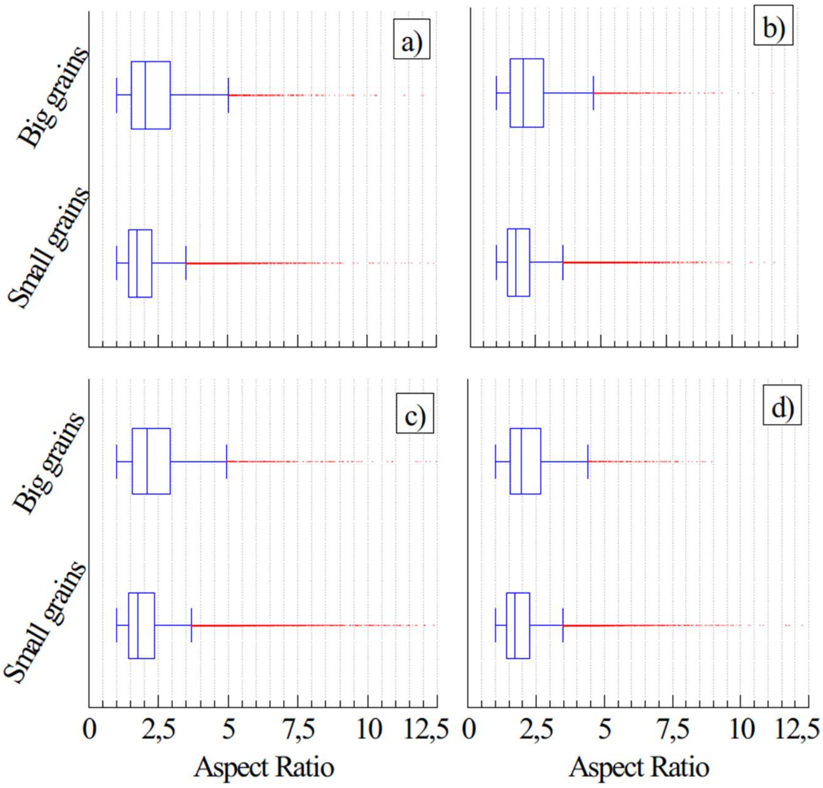

Figure 7: Whiskers diagrams of grain aspect ratio according to their type: a) S0; b) S45; c) S67; d) S90

Although from a general point of view, the texture of the microstructure is weak, we can guess local texture at a smaller scale. A first series of subsets of large columnar grains area (II) with the same inclination were isolated as illustrated in Fig 8 a). Then, as exhibited in Fig 8 b), the second family of grain size was also isolated by picking up one of two strips of small equiaxed grains (I). In this way, it allows us to study the grains coming from the same laser scanning direction.

Samples		S0		S45		S67		S90	
Area Analyzed (mm^3)		9,34		11,96		10,99		7,99	
Number of bead		7		10		7		6	
Maximum of Multiples of Uniform Density (MUD)		2,16		1,97		2,14		1,53	
Grain category		Small (I)	Coarse (II)	Small (I)	Coarse (II)	Small (I)	Coarse (II)	Small (I)	Coarse (II)
d_{eq}	Mean	7,91 ± 6,13	35,61 ± 11,92	7,16 ± 5,91	37,06 ± 12,93	6,95 ± 5,27	29,71 ± 12,80	7,59 ± 5,72	32,83 ± 8,44
	Median	5,7	37,09	4,79	32,98	5,2	25,78	5,7	30,16
Aspect ratio	Mean	1,73 ± 0,56	1,88 ± 0,76	1,75 ± 0,58	2,04 ± 0,89	1,75 ± 0,6	2,1 ± 0,95	1,73 ± 0,57	1,98 ± 0,79
	Median	1,74	1,64	1,66	1,87	1,65	1,91	1,64	1,83
Surface percentage		43	57	38	62	42	58	61	39
Number of grains percentage		91	9	91	9	94	6	95	5

Table 4: Statistical data taken from top surface EBSD maps

The microstructure (II) isolated in Fig 8 a) is composed of columnar grains having their ⟨011⟩ and ⟨111⟩ crystallographic direction aligned with the BD. The pole figures from the IPF Z highlight a strong {100} texture. A careful observation of the {100} pole figure reveals that {100} are not perfectly aligned with the sample reference. An approximate angle of 45° was measured between the BD direction and the maximum density. This result means that the fcc crystal lattice of the grains is tilted at 45° on the right. Also, on the same pole figure, the low-density semi-circle strip is evidence of a clear crystal rotation.

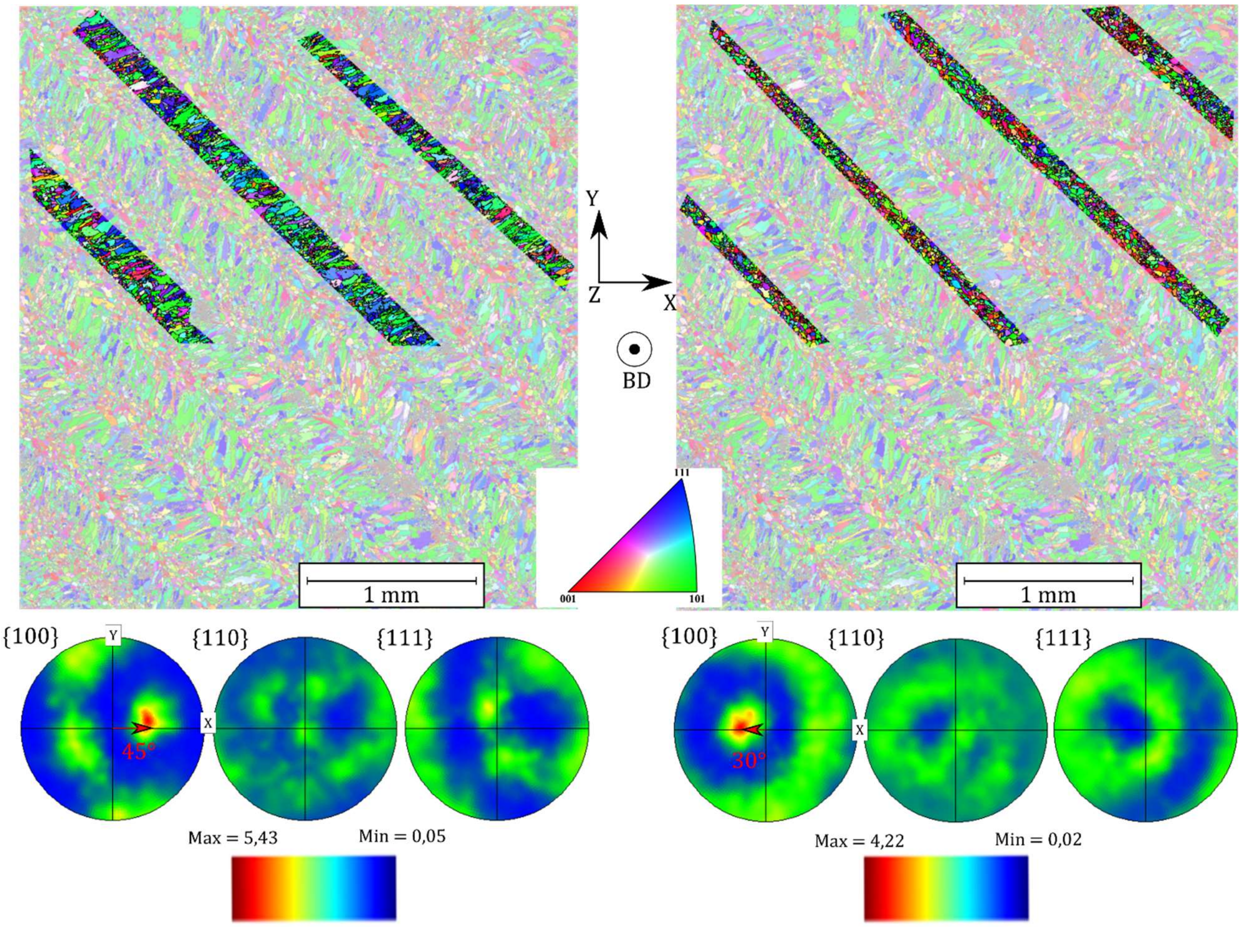

a)

b)

Figure 8: IPF Z showing the subsets taken off from the top surface of S45 and its pole figures: a) Large columnar grains subsets; b) Small equiaxed grains subsets

In the microstructure (I) exhibited in Fig 8 b), the microstructure is finer than the microstructure (II). It consists of small equiaxed grains having their ⟨001⟩ crystallographic directions aligned with the building direction. As well as for microstructure (II), a tilt and a rotation of the lattice can be observed. However, the tilt angle is slightly less substantial than in microstructure (II). Indeed, a tilt of 30° from the BD was measured. This result has been already reported by Balit et al. [42] by observing the transverse face microstructure of a 316L single bead wall.

Those top surface maps highlight the existence of a dual scale of microstructure texture which was not detected by analyzing the transverse microstructure. From a macroscopic scale, a non-textured microstructure is noticed whereas from a microscopic scale, whether we look at the microstructure on the side or in the middle of the bead, the latter is highly textured. Interestingly, Shao et al. [43], observed similar microstructure patterns when this alloy is manufactured by a powder bed process. They observed grains in the middle and on the side of the track having their ⟨001⟩ and ⟨011⟩ crystallographic directions respectively aligned with the BD. However, as the beads of this process are smaller than those from LMD, this phenomenon appears at a tinier scale and the grain size and morphology are different. Moreover, this AM process is thermally highly different compared to LMD. This one promotes even more epitaxial growth which leads to stronger texture [44]. Thus, despite their likeness, those microstructures differ on many points.

3.3 Microhardness

Hardness measurements on the top surface of the coating are finally performed. On average, the hardness values of top surface are 300 ± 9 HV, 292 ± 8 HV, 295 ± 10 HV and 305 ± 10 HV for the sample S0, S45, S67 and S90 respectively. Hence, the average hardness of the top surface is approximately the same no matter which coating strategy is used. For comparative purposes, hardness maps were also performed on a heat-treated wrought sample (955 °C/1h + 720 °C/8h + 620 °C/8h).

The smoothened contour plots of microhardness measurements are drawn in Fig 9 a), c), and e). Grains size map of the top surface of the S45 and S67 samples are illustrated in Fig 9 b) and d) respectively. Fig 9 f) displays the grains size map of the wrought sample. A hardness heterogeneity in the LMD samples is highlighted by the contour plot. The maximum hardness difference is 40 HV and 52 HV for S45 and S67 respectively. The wrought hardness is mainly included between 260 HV and 280 HV with an average of 273 ± 6 HV, which is in accordance with literature [25, 45], and is more homogeneous than LMD samples.

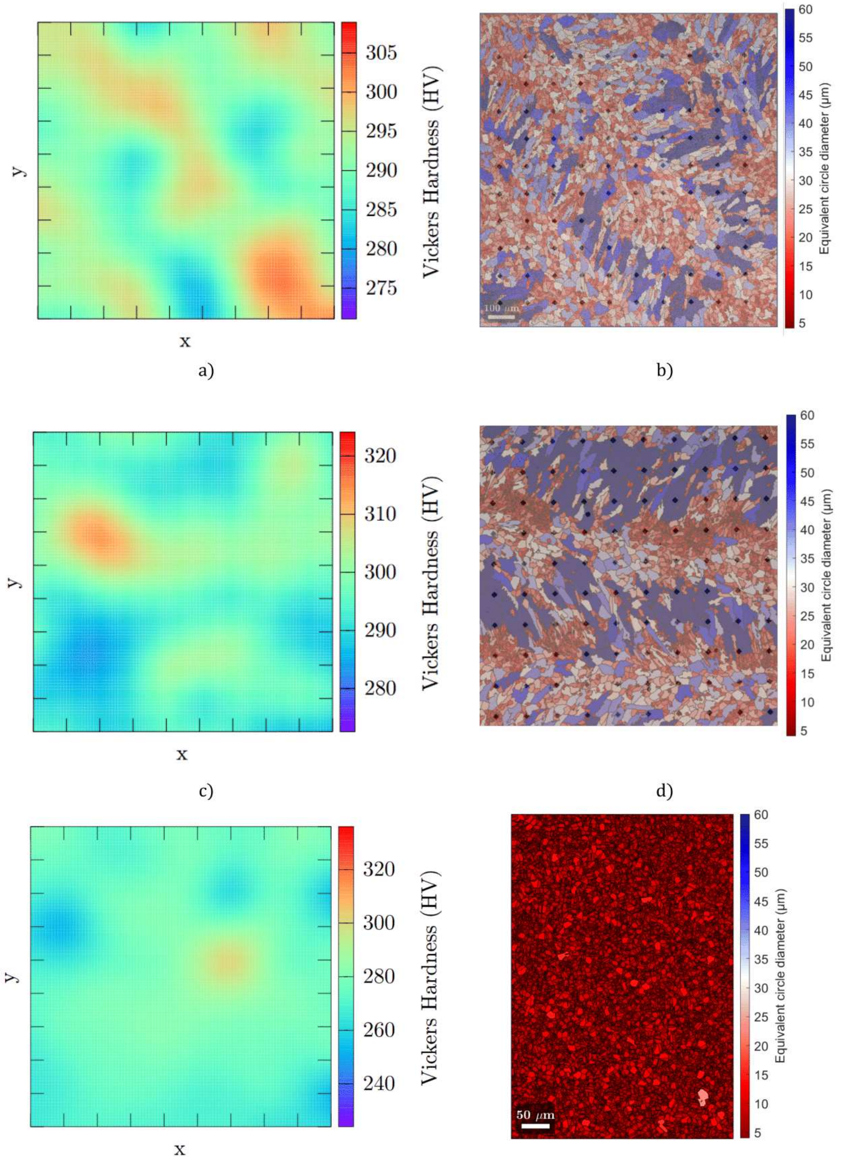

a)

b)

c)

d)

e)

f)

Figure 9: a), c) and e) Hardness contour plot on top surface microstructure of S45, S67 and wrought samples respectively (The authors want to specify that the highest hardness value in the wrought sample is due to the meeting between the indent and titanium nitrate (TiN)); b), d) and f) Maps of grains size of the top surface of S45, S67 and wrought samples respectively

Hardness profiles were also performed for each scanning strategy. Fig 10 gathers the four profiles. The hardness is constant according to the height in the coated area for all the samples. The value varies around an average hardness value of 310 HV. Once the profile crosses the coated area/substrate interface, the hardness increases sharply above 400 HV. Then, further into the substrate, the hardness decreases until reaching the classical hardness of the XC48 steel.

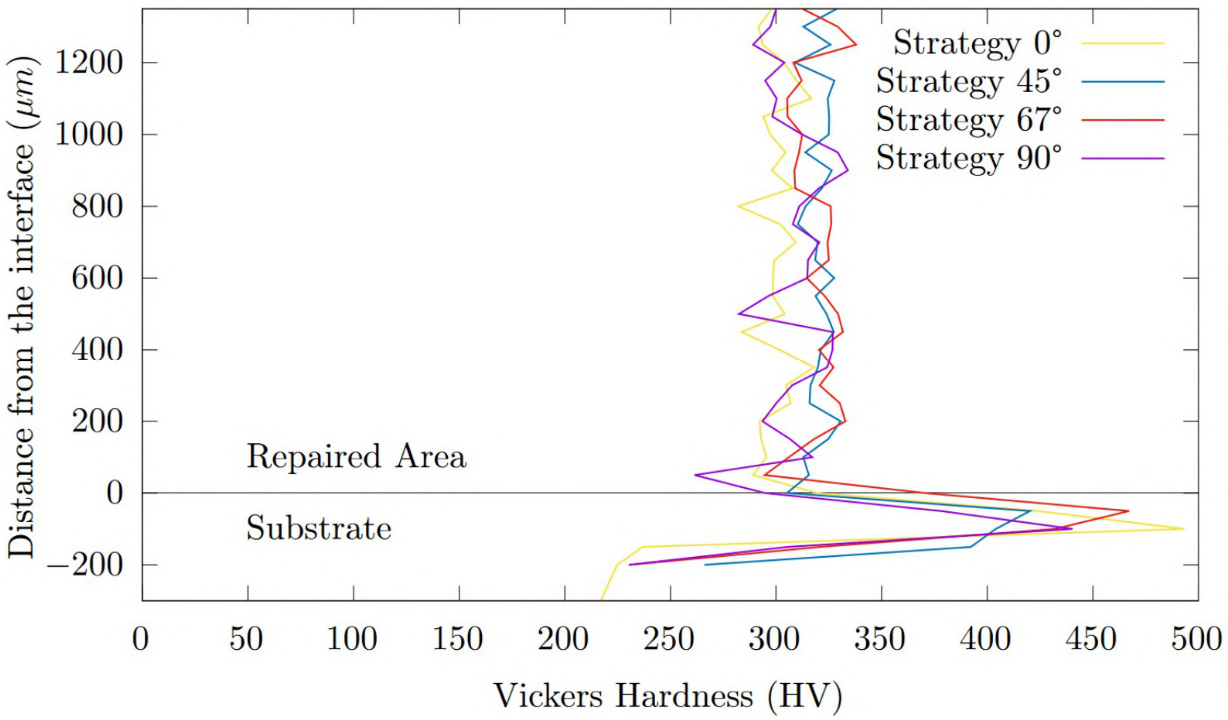

Figure 10: Hardness profile from the transversal face

4 Discussion

4.1 Lateral microstructures induced by LMD process

From a transversal point of view, the IN718 LMD microstructure is composed of two areas. The area close to the substrate (underneath the red dotted line in Fig 5 a)) is composed of elongated grains passing through several layers, whereas the upper area of the coating is composed of smaller grains restricted inside one layer. Furthermore, in the upper part of the coating, each layer is distinctly delimited by small grains. Those small grains in between deposited layers were already observed in LMD single bead walls in a few articles for different materials [14, 28] without being fully explained. This phenomenon may be explained as follows.

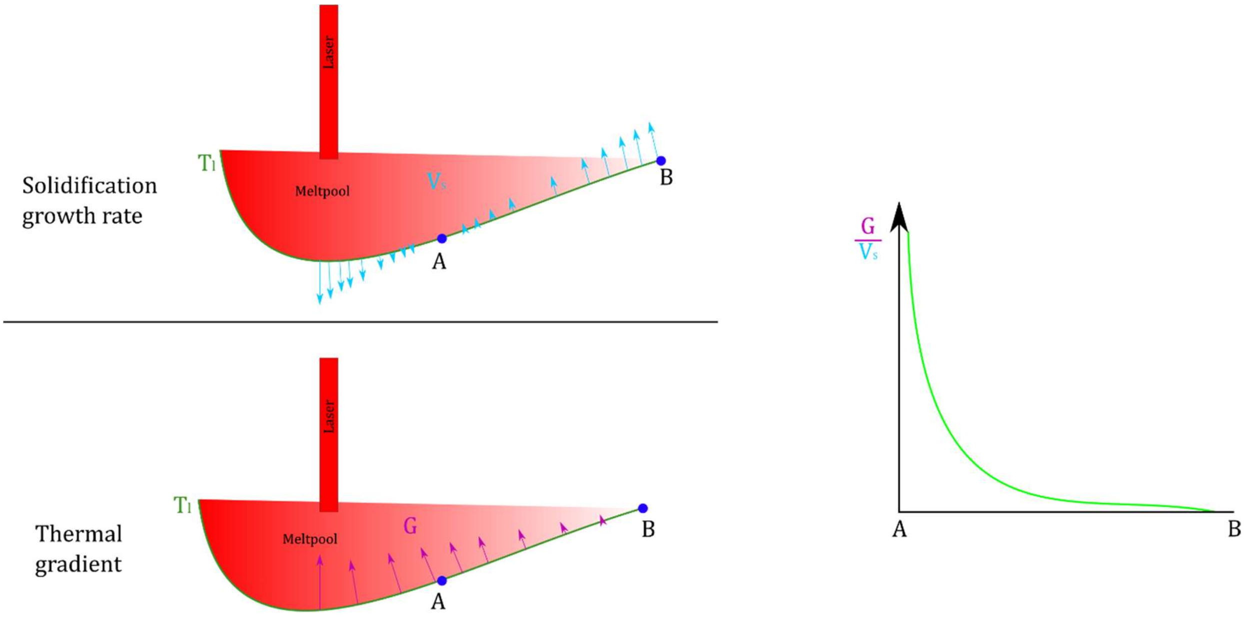

a) b)

Figure 11: a) Distribution of thermal gradient and solidification growth velocity at the liquid/solid interface of the meltpool; b) Evolution of the $\frac{G}{V_s}$ ratio along the liquid/solid interface at the rear of the meltpool

It is well known that the structure of the solidification front highly depends on the thermal gradient (G) and the liquid/solid interface velocity (V_s) [20, 46]. Depending on the location inside the melt pool, both are more or less substantial. As illustrated in Fig 11 a) thermal gradient is the largest under laser whereas the solidification front velocity increased when we get closer to the rear of the melt pool [46]. Blues arrows pointing down in Fig 11 a) signify material is melted by the laser so the solidification process is not started yet. The solidification process starts from point A. The liquid/solid interface velocity can be estimated as follows:

$$V_s = cos\theta \times V_{laser} \tag{1}$$

θ represents the angle between the growth direction vector and the laser scanning direction vector. The closer we get to the rear of the melt pool, the smaller the angle. Depending on the shape of the melt pool, the dendrite tip velocity can reach the laser scanning velocity which means that, in the latter case, the liquid/solid interface is perpendicular to the scanning direction. Hunt et al. [47] proposed a model which determines the columnar/equiaxed transition (CET) of the solidification front. According to Hunt et al., columnar growth can be hindered by the nucleation of equiaxed grains ahead of the solidification front in the undercooling area. It has been established that when the volume fraction of those equiaxed grains (ϕ_E) is below 0.66% a fully columnar microstructure is obtained. ϕ_E is related to the nucleation undercooling (ΔT_n) and the density of nucleation sites (N_e) which are directly linked with G and V_S. Considering Hunt's model, CET happens when:

$$\left(\frac{G}{\sqrt[n]{\frac{V_S}{A}}}\right) < 0.617N_e^{\frac{1}{3}} \tag{2}$$

with A and n corresponding to growth parameters. Equation 2 shows that if the ratio G/V_S is low enough CET happens. By investigating the CET transition in IN718 during LMD, Lv et al. [48] showed that the latter transition happens in LMD but it can be delayed by moving the process parameters. As shown in Fig 11 b), G/V_S is the lowest at the rear of the melt pool. Thus, CET is more likely to happen at the rear of the melt pool which translates into a layer of small equiaxed grains at the top of the bead. Whether the AM process used is an LPBF process or a DED process, a thin layer of equiaxed grains is often observed at the top of the bead in the literature [28]. A convection component could also explain the small grain at the surface of the bead [20]. However, conduction mainly drives the cooling, even more in a three-dimensional coating. Therefore, this assumption is less likely to happen. At the very top of the as-build samples, a layer of 60 μm height on average of small equiaxed grains was measured as shown in Fig 12 b). Given the significant height of this layer, the epitaxial growth may be hindered by the latter as observed in Fig 5 a). Indeed, if the dilution of the bead in the previously deposited layer is not enough to remelt the whole small grain layer, then epitaxial growth is impeded. However, this phenomenon does not happen for the first three layers. The most likely reason comes from the high thermal gradient caused by the cold substrate. Indeed, as the substrate is not pre-heated, when the first layers are deposited, the molten alloy is subjected to a considerable thermal gradient which, according to Hunt's model, would delay the CET. Thus, the first layers deposited might have a thin layer of small grain on their top which can be easily remelted. As the coating goes up, heat accumulates, which decreases significantly G. Thus, as the G/V_S lowers, the equiaxed grains layer height increases and hinders the epitaxial growth. Nonetheless, long columnar grains passing through several layers are sporadically observed in Fig 12 a) at the top of the coating. In addition to the drop of G, during the building of the last layers, the overall temperature of the part reaches high values which results in a bigger melt pool. By being larger, the melt pool may easily melt the entirety of the obstructing layer and consequently promotes epitaxial growth. Furthermore, as observed in Fig12 b), the thickness of the strip of small grains is unsteady which explains the irregular nature of this phenomenon. Also, unmelted particles at the top of the bead can favor the unsteadiness of the strip. It is worth noting that no matter which strategy is used; those events happen anyway. It also must be noted in Fig 12 c), that a strong texture is noticed in the longitudinal transverse view of S0. This is specific to this sample because of the constant scanning direction imposed by the scanning strategy. However, because of the rotation of the scanning direction, the other samples display a much lower texture which never exceeds 1.74. The S45, S67, and S90 microstructures may be interesting because it reduces the inherent anisotropic mechanical properties of as-build LMD coatings.

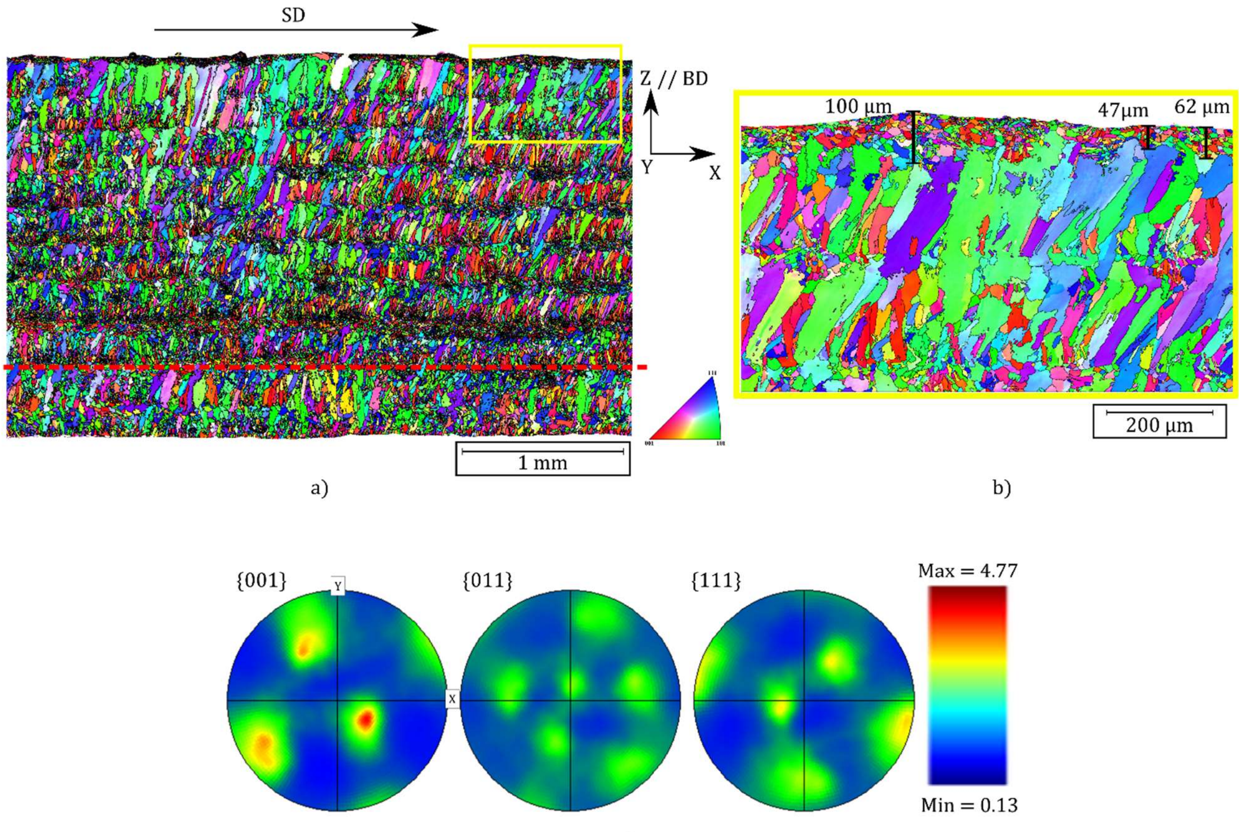

a)

b)

c)

Figure 12: a) IPF Z showing the subsets taken off from the longitudinal transverse surface of S0 ; b) A zoomed-in area highlighting the layer composed of small grains; c) Pole figures of unzoomed longitudinal transverse EBSD map

4.2 Top surface microstructure induced by LMD process

Top surface EBSD results presented in Fig 6 showed a heterogeneous microstructure consisting of an alternation of small equiaxed grains and large columnar grains with a pronounced local texture. The origins of such an observation have to be better understood because microstructure may have a great impact on the tribological properties of the coating.

As AM processes are thermally close to welding, some similar microstructure features can be observed [41]. Unlike conventional processes such as casting, laser cladding favor the epitaxial growth of grains from the adjacent layers. As a general rule, the solidification front follows the heat flow. The latter is greatly dependent on the scanning parameter and thermal fields inside the melt pool. Thus, depending on the process parameters, the shape of the melt pool will change [20]. During melt pool solidification, the surrounding solid acts as a heat sink leading to directional solidification. The growth direction is opposite to the maximal temperature gradient which is perpendicular to the liquid-solid interface of the melt pool. Since the face-centered cubic matrix γ has a preferential growth direction according to the ⟨100⟩ crystallographic direction [49], dendrites' primary arms grow with this crystallographic direction aligned with the effective heat flow direction. As shown in Fig 5 b), in the middle of the bead, most of the grains have their ⟨100⟩ directions oriented alongside the BD because the heat flow is oriented in the same opposite direction. It explains why most of the grains in microstructure (I) have their ⟨100⟩ aligned with BD. The 30° angle offset of the {001} planes from the BD observed on the pole figure in Fig 8 b) may be explained by the longitudinal view A-A in Fig 13). As the maximal thermal gradient is aligned with the BD [41], the only rotation of the lattice is imposed by the longitudinal shape of the melt pool. Although the precise shape of the melt pool was not calculated or measured during printing, we can guess through the {001} pole figure that the thermal gradient is tilted by 30° from the BD.

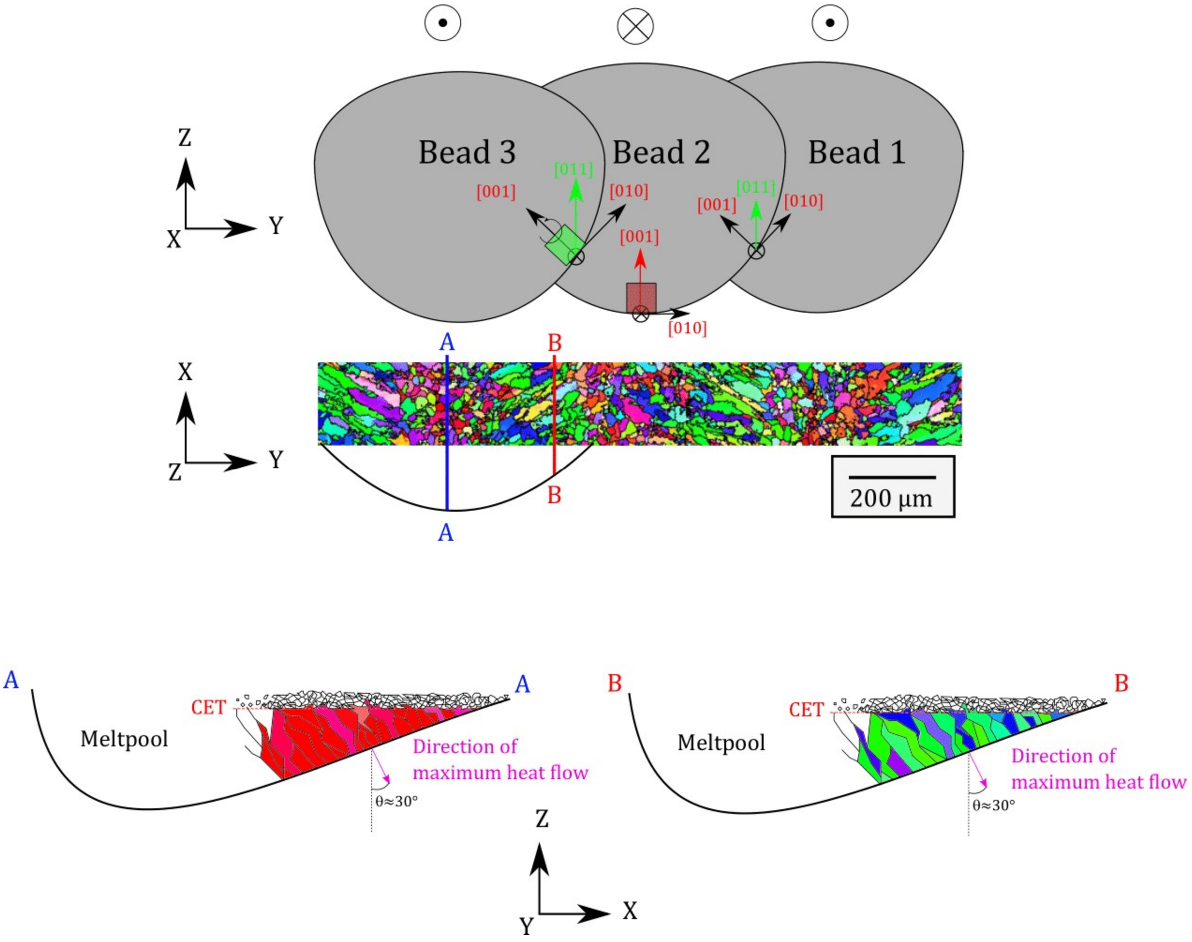

Figure 13: Explanatory drawing of the typical texture of LMD coatings

Then, by moving away from the middle of the bead, the direction of the steepest temperature gradient will gradually rotate because of the U-shape of the melt pool leading to the inclination of the growth solidification front as well. As explained in Fig 13, if the crystal lattice is rotated by 45° as observed in Fig 8 a), it aligns the ⟨011⟩ directions with the BD. This explains the strong {001} texture located in (II) with an offset angle of 45° with the BD. However, the high number of grains with a ⟨111⟩ texture is still not fully understood. Our main assumption can be explained through the transversal and longitudinal view B-B of the bead displayed in Fig 13. It seems that on the side, the ⟨011⟩ // BD and ⟨111⟩ // BD texture is most likely due to a competition between the heat flow induced by the transversal and longitudinal shape of the melt pool. Thus, by adding a rotation around the Y axe to the already 45°rotated lattice, it may justify the slight ⟨111⟩ // BD texture observed in the IPF Z map of the top surface. Shao et al. [43] also observed in the overlap area a texture ⟨111⟩ // BD with the LPBF process when the overlap rate exceeds 50%.

To conclude, interestingly, the microstructure of the four scanning strategies are similar despite their different thermal cycles. Statistic study shows their high similitude in terms of microstructural features. As demonstrated in Fig 13, the middle of the beads is composed of small equiaxed grains having their ⟨100⟩ crystallographic directions aligned with the BD while the bead's sides are composed of the elongated grains having ⟨110⟩ and ⟨111⟩ directions mostly aligned with the BD. By correlating with transverse microstructure, the equiaxed grains located in the middle of the bead (I) are nothing else than columnar grains observed from the top. Finally, because of the curved geometry of the melt pool, columnar grains close to the bead border (II) are tilted and stand out as elongated grains from this point of view.

4.3 Coatings hardness

Fig 9 displays the heterogeneity of the top surface hardness of IN718 LMD coating. By comparing the hardness pattern with the associated microstructure, a clear relationship between both is highlighted. Indeed, the hardness is the most significant in the area of the small grain which is due to the capacity of the grain boundaries to hinder the movement of the dislocations. The finer the microstructure, the greater the density of grain boundaries, which leads to an increase of the hardness [50]. Thus, the periodic heterogeneous grain size leads to non-uniform hardness with a pattern. On the other hand, as displayed in Fig 9 f) the wrought sample has a homogeneous microstructure composed of fine equiaxed grains with an average size of 4,27 ± 0,83 μm.

The mean hardness of coatings is higher compared to the hardness of the wrought sample presented in Fig 9 e) which is close to 270 HV. The main reason is the presence of high dislocation density near the wall of the cell of the sub-microstructure [45, 51]. So, even after a proper heat treatment which dissolves the detrimental phases in the matrix and precipitates the strengthening phases, wrought specimens still have a lower hardness with its almost dislocation-free recrystallized fine microstructure. Moreover, no strengthening phases were observed in the microstructure. Only Laves phases and microsegregation of heavy elements (Nb and Mo especially) were noticed inside the interdendritic region. Hence, if we compare the hardness of those two processes, even though the heat-treated wrought sample has a finer microstructure and probably γ'/γ'' strengthening phases inside its austenitic matrix, the hardness of the wrought sample is lower than the LMD samples.

However, by comparing our LMD samples built with the same process parameters, we can assume they have approximately the same amount of dislocation in their cell walls. Table 4 also demonstrates how similar the overall LMD microstructures are similar despite their different scanning strategy. Thus, the heterogeneity of hardness at the top of IN718 coating is assumed to be mainly caused by the amount of grain boundaries meet by the Vickers indent.

A heterogeneous hardness leads to non-uniform mechanical properties which can particularly affect the tribological properties of the surface. Studies on the Laser-PBF process showed anisotropic wear behavior of as-build pieces and presented better mechanical properties than conventional process [29, 30, 52]. Those results open the possibility to tailor optimized hardness patterns by playing with the scanning path.

As exhibited in Fig 10, from a transversal point of view, hardness in the coated area along the building direction is much more constant compared to the top surface. It demonstrates that, for relatively low coating height, the scanning strategy does not affect the average hardness all along the building direction. Stevens et al. [18] observed conversely a hardness variation. In our case, the coating height is too small to observe such a trend. A similar trend might be expected if a higher coating is printed. Indeed, the accumulation of heat and the lower number of thermal cycles induced by the repeated laser passing would decrease the cooling temperature leading to a coarser microstructure with fewer strengthening phases [53].

The sharp increase of the hardness close to the repaired area/substrate interface can be easily explained by the hard martensitic microstructure of the substrate close to the interface. When the first layer is deposited, the laser melts also the top surface of the XC48 substrate which leads to a martensitic microstructure because of the high cooling rate. By going deeper into the substrate, the hardness profile takes away from the heat-affected zone. The last indentations in the substrate are located in the classical ferritic-perlitic microstructure of the steel substrate which ensues a decrease in hardness.

5 Conclusions and perspectives

Our goal was to investigate the microstructure of a 3D IN718 coating simulating the repair of a large defect. We focused on top-surface microstructures which is most likely to be exposed to the stresses caused by mechanical contact but also, interestingly, generally not studied in the literature. In this paper, we investigated samples fabricated by LMD process using different scanning strategies. First, we investigated the density of our samples for different building strategies. Then, we characterized them by analyzing the EBSD maps from different angles. Finally, we performed hardness measurements to estimate the changes in mechanical properties. The main conclusions of this work can be summarized as follows:

- Four coatings with different scanning strategies were successfully fabricated with high density (estimated by image analysis around 99.9%) and with no differences in terms of microstructural features.

- From a transverse view, layers of the coatings with small equiaxed grains between them are clearly visible.

- Top surface coating microstructure consists of an alternation of small equiaxed grains and large elongated grains with an average grain size of about 7 and 35 μm, respectively. Statistics confirm that larger grains are mainly columnar and smaller grains are equiaxed.

- The coating top surfaces show a double-scale microstructural texture. At the macroscopic level, the texture appears to be weak (with a maximum of multiples of uniform density (MUD) ≤ 2), while at the microscopic level it is strong (max MUD ≥ 4) and varies according to localization within a bead. The latter was explained by the direction of the maximum thermal gradient, the shape of the melt pool, and the preferred crystallographic grain growth direction.

- The pronounced heterogeneity of the microstructure leads to a clear hardness heterogeneity, the pattern of which is directly linked to the scanning strategy.

- With an average hardness of about 310 HV, the LMD samples were found to be harder than heat-treated wrought samples (270 HV). These results are promising for the wear resistance of parts repaired by LMD.

This article has shown that the LMD process is capable of affecting the surface hardness of its coatings through the microstructure, and reveals its high competitiveness in terms of hardness compared to a conventional process. These initial results promise further important steps in LMD-based repair process with good wear resistance surfaces ; further studies are under progress to determine the wear resistance of these coatings.

6 Data Availability

The raw/processed data required to reproduce these findings cannot be shared at this time as the data also forms part of an ongoing study.

7 Conflicts of interest

The authors declare no conflicts of interest.

8 Acknowledgments

Those researches were founded by the *Société nationale des chemins de fer français* (SNCF, France) and the *Direction Générale de l'Armement* (DGA, France). The authors want to thank Benoit Dodin (SNCF) and Marie-Christine Sainte Catherine (DGA) for their fruitful discussions. A warm thanks to Simon Hallais, Alexandre Tanguy and Pierre-Louis Hanappier for assisting with the SEM measurements and manufacturing samples.

References

[1] N. Curry et al. “Evaluation of the lifetime and thermal conductivity of dysprosia-stabilized thermal barrier coating systems”. In: *Journal of Thermal Spray Technology* 22.6 (2013), pp. 864–872. issn: 10599630. doi: 10.1007/s11666-013-9932-9.

[2] T. Alvarez Tejedor, R. Singh, and P. Pilidis. *Maintenance and repair of gas turbine components*. Woodhead Publishing, 2013, pp. 565–634. isbn: 9781845697280. doi: 10.1533/9780857096067.3.565.

[3] D. Peng et al. “On the role of the interface on the damage tolerance and durability of cold spray repairs to AA7075-T7351 aluminium alloy wing skins”. In: *Applied Surface Science Advances* 3.October 2020 (2021), p. 100044. issn: 26665239. doi: 10.1016/j.apsadv.2020.100044. url: https://doi.org/10.1016/j.apsadv.2020.100044.

[4] B. Graf, A. Gumenyuk, and M. Rethmeier. “Laser Metal Deposition as Repair Technology for Stainless Steel and Titanium Alloys”. In: *Physics Procedia* 39 (2012), pp. 376–381. issn: 18753892. doi: 10.1016/j.phpro.2012.10.051. url: http://dx.doi.org/10.1016/j. phpro.2012.10.051.

[5] V. Ocelik et al. “Thick Co-based coating on cast iron by side laser cladding: Analysis of processing conditions and coating properties”. In: *Surface and Coatings Technology* 201.12 (2007), pp. 5875–5883. issn: 02578972. doi: 10.1016/j.surfcoat.2006.10.044.

[6] J. M. Wilson et al. “Remanufacturing of turbine blades by laser direct deposition with its energy and environmental impact analysis”. In: *Journal of Cleaner Production* 80 (2014), pp. 170–178. issn: 09596526. doi: 10.1016/j.jclepro.2014.05.084. url: http://dx.doi.org/10.1016/j.jclepro.2014.05.084.

[7] H. Liu et al. “Parameter optimization and experimental study of the sprocket repairing using laser cladding”. In: *International Journal of Advanced Manufacturing Technology* 91.9-12 (2017), pp. 3967–3975. issn: 14333015. doi: 10.1007/s00170-017-0066-y.

[8] G. Bi and A. Gasser. “Restoration of nickel-base turbine blade knife-edges with controlled laser aided additive manufacturing”. In: *Physics Procedia* 12.PART 1 (2011), pp. 402–409. issn: 18753892. doi: 10.1016/j.phpro.2011.03.051. url: http://dx.doi.org/10.1016/ j.phpro.2011.03.051.

[9] T. Unal-Saewe et al. “Process development for tip repair of complex shaped turbine blades¨ with IN718”. In: *Procedia Manufacturing* 47.2019 (2020), pp. 1050–1057. issn: 23519789. doi: 10.1016/j.promfg.2020.04.114. url: https://doi.org/10.1016/j.promfg.2020.04.114.

[10] M. D. Sangid et al. “Role of heat treatment and build orientation in the microstructure sensitive deformation characteristics of IN718 produced via SLM additive manufacturing”. In: *Additive Manufacturing* 22 (Aug. 2018), pp. 479–496. issn: 2214-8604. doi: 10.1016/J. ADDMA.2018.04.032. url: https://www.sciencedirect.com/science/article/pii/ S2214860418300472.

[11] T. M. Pollock and S. Tin. “Nickel-based superalloys for advanced turbine engines: Chemistry, microstructure, and properties”. In: *Journal of Propulsion and Power* 22.2 (2006), pp. 361– 374. issn: 15333876. doi: 10.2514/1.18239.

[12] Y. Zhang et al. “Effect of cooling rate on the microstructure of laser-remelted INCONEL 718 coating”. In: *Metallurgical and Materials Transactions A: Physical Metallurgy and Materials Science* 44.12 (2013), pp. 5513–5521. issn: 10735623. doi: 10.1007/s11661-013-1903-8.

[13] G. P. Dinda, A. K. Dasgupta, and J. Mazumder. “Laser aided direct metal deposition of Inconel 625 superalloy: Microstructural evolution and thermal stability”. In: *Materials Science and Engineering A* 509.1-2 (2009), pp. 98–104. issn: 09215093. doi: 10.1016/j.msea.2009. 01.009.

[14] L. L. Parimi et al. “Microstructural and texture development in direct laser fabricated IN718”. In: *Materials Characterization* 89 (2014), pp. 102–111. issn: 1044-5803. doi: https://doi.org/10.1016/j.matchar.2013.12.012. url: http://www.sciencedirect.com/science/article/pii/S1044580313003835.

[15] Q. Zhang, J. Yao, and J. Mazumder. “Laser Direct Metal Deposition Technology and Microstructure and Composition Segregation of Inconel 718 Superalloy”. In: *Journal of Iron and Steel Research, International* 18 (Apr. 2011), pp. 73–78. doi: 10.1016/S1006-706X(11) 60054-X.

[16] C. Zhong et al. “Microstructures and tensile properties of Inconel 718 formed by high depositionrate laser metal deposition”. In: *Journal of Laser Applications* 28.2 (2016), p. 022010. issn:
1042-346X. doi: 10.2351/1.4943290. url: http://dx.doi.org/10.2351/1.4943290.

[17] R. G. Ding et al. “Electron microscopy study of direct laser deposited IN718”. In: *Materials Characterization* 106 (2015), pp. 324–337. issn: 10445803. doi: 10.1016/j.matchar.2015. 06.017.

[18] E. L. Stevens et al. “Variation of hardness, microstructure, and Laves phase distribution in direct laser deposited alloy 718 cuboids”. In: *Materials and Design* 119 (2017), pp. 188–198. issn: 18734197. doi: 10.1016/j.matdes.2017.01.031. url: http://dx.doi.org/10.1016/j.matdes.2017.01.031.

[19] M. Ma, Z. Wang, and X. Zeng. “Effect of energy input on microstructural evolution of direct laser fabricated IN718 alloy”. In: *Materials Characterization* 106 (Aug. 2015), pp. 420– 427. issn: 1044-5803. doi: 10.1016/J.MATCHAR.2015.06.027. url: https://www.sciencedirect.com/science/article/pii/S1044580315002338.

[20] C. Gu´evenoux et al. “Influence of interlayer dwell time on the microstructure of Inconel 718 Laser Cladded components”. In: *Optics and Laser Technology* 128.March (2020), p. 106218. issn: 00303992. doi: 10.1016/j.optlastec.2020.106218. url: https://doi.org/10.1016/j.optlastec.2020.106218.

[21] K. Yuan et al. “Influence of process parameters and heat treatments on the microstructures and dynamic mechanical behaviors of Inconel 718 superalloy manufactured by laser metal deposition”. In: *Materials Science and Engineering A* 721.February (2018), pp. 215–225. issn: 09215093. doi: 10.1016/j.msea.2018.02.014.

[22] Z. Yang et al. “Effects of ultrasound on multilayer forming mechanism of Inconel 718 in directed energy deposition”. In: *Additive Manufacturing* 48.PB (2021), p. 102462. issn: 22148604. doi: 10.1016/j.addma.2021.102462. url: https://doi.org/10.1016/j.addma.2021. 102462.

[23] Lida Zhu et al. “Microstructure and mechanical properties of parts formed by ultrasonic vibration-assisted laser cladding of Inconel 718”. In: *Surface and Coatings Technology* 410.January (2021), p. 126964. issn: 02578972. doi: 10.1016/j.surfcoat.2021.126964. url: https://doi.org/10.1016/j.surfcoat.2021.126964.

[24] S. Sui et al. “The influence of Laves phases on the high-cycle fatigue behavior of laser additive manufactured Inconel 718”. In: *Materials Science and Engineering A* 695.March (2017), pp. 6–13. issn: 09215093. doi: 10.1016/j.msea.2017.03.098. url: http://dx.doi.org/10.1016/j.msea.2017.03.098.

[25] J. Nguejio et al. “Comparison of microstructure features and mechanical properties for additive manufactured and wrought nickel alloys 625”. In: *Materials Science and Engineering A* 764.Julyg (2019), p. 138214. issn: 09215093. doi: 10.1016/j.msea.2019.138214. url: https://doi.org/10.1016/j.msea.2019.138214.

[26] I. Tabernero et al. “Evaluation of the mechanical properties of Inconel 718 components built by laser cladding”. In: *International Journal of Machine Tools and Manufacture* 51.6 (2011), pp. 465–470. issn: 08906955. doi: 10.1016/j.ijmachtools.2011.02.003.

[27] P. L. Blackwell. “The mechanical and microstructural characteristics of laser-deposited IN718”. In: *Journal of Materials Processing Technology* 170.1-2 (2005), pp. 240–246. issn: 09240136. doi: 10.1016/j.jmatprotec.2005.05.005.

[28] Y. Balit, E. Charkaluk, and A. Constantinescu. “Digital image correlation for microstructural analysis of deformation pattern in additively manufactured 316L thin walls”. In: *Additive Manufacturing* 31.September 2019 (2020), p. 100862. issn: 22148604. doi: 10.1016/j.addma.2019.100862. url: https://doi.org/10.1016/j.addma.2019.100862.

[29] M. Bahshwan et al. “The role of microstructure on wear mechanisms and anisotropy of additively manufactured 316L stainless steel in dry sliding”. In: *Materials and Design* 196 (2020), p. 109076. issn: 18734197. doi: 10.1016/j.matdes.2020.109076. url: https://doi.org/10.1016/j.matdes.2020.109076.

[30] Y. Yang et al. “Wear anisotropy of selective laser melted 316L stainless steel”. In: *Wear* 428429.January (2019), pp. 376–386. issn: 00431648. doi: 10.1016/j.wear.2019.04.001. url: https://doi.org/10.1016/j.wear.2019.04.001.

[31] AddUp Company. *BeAM*. url: https://www.beam-machines.fr/.

[32] Oerlikon. *Oerlikon AM*. url: https://www.oerlikon.com/am/en/offerings/metalpowders/ (cit. on p. 6).

[33] B. Bax et al. “Systematic evaluation of process parameter maps for laser cladding and directed energy deposition”. In: *Additive Manufacturing* 21.January (2018), pp. 487–494. issn: 22148604. doi: 10.1016/j.addma.2018.04.002. url: https://doi.org/10.1016/j.addma. 2018.04.002.

[34] T. Bhardwaj et al. “Direct Energy Deposition - Laser Additive Manufacturing of TitaniumMolybdenum alloy: Parametric studies, microstructure and mechanical properties”.

In: *Journal of Alloys and Compounds* 787 (2019), pp. 1238–1248. issn: 09258388. doi: 10.1016/j.jallcom.2019.02.121. url: https://doi.org/10.1016/j.jallcom.2019.02.121.

[35] N. Nadammal et al. "Critical role of scan strategies on the development of microstructure, texture, and residual stresses during laser powder bed fusion additive manufacturing". In: *Additive Manufacturing* 38.December 2020 (2021), p. 101792. issn: 22148604. doi: 10.1016/j.addma.2020.101792. url: https://doi.org/10.1016/j.addma.2020.101792.

[36] I. Serrano-Munoz et al. "Scanning Manufacturing Parameters Determining the Residual Stress State in LPBF IN718 Small Parts". In: *Advanced Engineering Materials* (2021). issn: 15272648. doi: 10.1002/adem.202100158.

[37] X. Zhang et al. "Effect of the scanning strategy on microstructure and mechanical anisotropy of Hastelloy X superalloy produced by Laser Powder Bed Fusion". In: *Materials Characterization* 173.December 2020 (2021), p. 110951. issn: 10445803. doi: 10.1016/j.matchar.2021.110951. url: https://doi.org/10.1016/j.matchar.2021.110951.

[38] Oxford Instruments. *Oxford Instruments*. url: https://www.oxinst.com/.

[39] S. Wang et al. "Role of porosity defects in metal 3D printing: Formation mechanisms, impacts on properties and mitigation strategies". In: *Materials Today* 59.October (2022), pp. 133–160. issn: 18734103. doi: 10.1016/j.mattod.2022.08.014. url: https://doi.org/10.1016/j. mattod.2022.08.014.

[40] Y. R. Choi et al. "Influence of deposition strategy on the microstructure and fatigue properties of laser metal deposited Ti-6Al-4V powder on Ti-6Al-4V substrate". In: *International Journal of Fatigue* 130.December 2018 (2020), p. 105236. issn: 01421123. doi: 10.1016/j.ijfatigue.2019.105236. url: https://doi.org/10.1016/j.ijfatigue.2019.105236.

[41] S. A. David and J. M. Vitek. "Correlation between solidification parameters and weld microstructures". In: *International Materials Reviews* 34.1 (1989), pp. 213–245. issn: 17432804. doi: 10.1179/imr.1989.34.1.213.

[42] Y. Balit et al. "Self-heating behavior during cyclic loadings of 316L stainless steel specimens manufactured or repaired by Directed Energy Deposition To cite this version : HAL Id : hal-02563296 Self-heating behavior during cyclic loadings of 316L stainless steel specime". In: (2020).

[43] W. Shao et al. "Effect of hatch spacing and laser remelting on the formation of unique crystallographic texture of IN718 superalloy fabricated via laser powder bed fusion". In: *Optics and Laser Technology* 156.August (2022), p. 108609. issn: 00303992. doi: 10.1016/j.optlastec.2022.108609. url: https://doi.org/10.1016/j.optlastec.2022.108609
.

[44] H. Y. Wan et al. "Effect of scanning strategy on grain structure and crystallographic texture of Inconel 718 processed by selective laser melting". In: *Journal of Materials Science & Technology* 34.10 (2018), pp. 1799–1804. issn: 1005-0302. doi: https://doi.org/10.1016/ j.jmst.2018.02.002. url: http://www.sciencedirect.com/science/article/pii/ S1005030218300252.

[45] Y. Zhao et al. "Comparative study on the microstructure evolution of selective laser melted and wrought IN718 superalloy during subsequent heat treatment process and its effect on

mechanical properties”. In: *Materials Science and Engineering A* 791.June (2020), p. 139735. issn: 09215093. doi: 10.1016/j.msea.2020.139735. url: https://doi.org/10.1016/j.msea.2020.139735.

[46] D. Guo et al. “Solidification microstructure and residual stress correlations in direct energy deposited type 316L stainless steel”. In: *Materials and Design* 207 (2021), p. 109782. issn: 18734197. doi: 10.1016/j.matdes.2021.109782. url: https://doi.org/10.1016/j.matdes.2021.109782.

[47] J. D. Hunt. “Steady state columnar and equiaxed growth of dendrites and eutectic”. In: *Materials Science and Engineering* (1984). issn: 00255416. doi: 10.1016/0025-5416(84) 90201-5.

[48] H. Lv et al. “Investigation on the columnar-to-equiaxed transition during laser cladding of IN718 alloy”. In: *Journal of Manufacturing Processes* 67.April (2021), pp. 63–76. issn: 15266125. doi: 10.1016/j.jmapro.2021.04.016. url: https://doi.org/10.1016/j. jmapro.2021.04.016.

[49] S .A. David et al. “Application of single crystals to achieve quantitative understanding of weld microstructures”. In: *Materials Science and Technology* 11.9 (Sept. 1995), pp. 939–948. issn: 0267-0836. doi: 10.1179/mst.1995.11.9.939. url: https://doi.org/10.1179/mst.1995. 11.9.939.

[50] N. Hansen. “Hall-petch relation and boundary strengthening”. In: *Scripta Materialia* 51.8 SPEC. ISS. (2004), pp. 801–806. issn: 13596462. doi: 10.1016/j.scriptamat.2004.06.002.

[51] W. M. Tucho et al. “Microstructure and hardness studies of Inconel 718 manufactured by selective laser melting before and after solution heat treatment”. In: *Materials Science and Engineering A* 689.February (2017), pp. 220–232. issn: 09215093. doi: 10.1016/j.msea.2017.02.062. url: http://dx.doi.org/10.1016/j.msea.2017.02.062.

[52] M. Bahshwan et al. “In situ observation of anisotropic tribological contact evolution in 316L steel formed by selective laser melting”. In: *Wear* 490-491.November 2021 (2022), p. 204193. issn: 00431648. doi: 10.1016/j.wear.2021.204193. url: https://doi.org/10.1016/j.wear.2021.204193.

[53] Y. Tian et al. “Rationalization of microstructure heterogeneity in INCONEL 718 builds made by the direct laser additive manufacturing process”. In: *Metallurgical and Materials Transactions A: Physical Metallurgy and Materials Science* 45.10 (2014), pp. 4470–4483. issn: 10735623. doi: 10.1007/s11661-014-2370-6.